Shear sensor mechano-signaling determines tendon stiffness and human jumping performance

Fabian S. Passini
University Hospital Balgrist, University of Zurich / Institute for Biomechanics, ETH Zurich
https://orcid.org/0000-0002-1258-4002

Patrick K. Jaeger
University Hospital Balgrist, University of Zurich / Institute for Biomechanics, ETH Zurich

Aiman S. Saab
Institute of Pharmacology and Toxicology, University of Zurich / Neuroscience Center, University and ETH Zurich

Shawn Hanlon
Department of Physical Therapy, University of Delaware

Matthias Arlt
University Hospital Balgrist, University of Zurich / Institute for Biomechanics, ETH Zurich

Kim David Ferrari
Institute of Pharmacology and Toxicology, University of Zurich / Neuroscience Center, University and ETH Zurich

Nicole Chittim
University Hospital Balgrist, University of Zurich / Institute for Biomechanics, ETH Zurich

Dominik Haenni
Center for Microscopy and Image Analysis, University of Zurich

Sebastiano Caprara
University Hospital Balgrist, University of Zurich / Institute for Biomechanics, ETH Zurich

Maja Bollhalder
University Hospital Balgrist, University of Zurich / Institute for Biomechanics, ETH Zurich

Aron Horvath
University Hospital Balgrist, University of Zurich / Institute for Biomechanics, ETH Zurich

Tobias Goetschi
University Hospital Balgrist, University of Zurich / Institute for Biomechanics, ETH Zurich

Shang Ma
Howard Hughes Medical Institute, Department of Neuroscience, Dorris Neuroscience Center, Scripps Research

Bettina Passini-Tall
University Hospital Balgrist, University of Zurich / Institute for Biomechanics, ETH Zurich

Sandro Fucentese

University Hospital Balgrist, University of Zurich / Institute for Biomechanics, ETH Zurich

Ulrich Blache

University Hospital Balgrist, University of Zurich / Institute for Biomechanics, ETH Zurich

Unai Silvan

University Hospital Balgrist, University of Zurich / Institute for Biomechanics, ETH Zurich

Bruno Weber

Institute of Pharmacology and Toxicology, University of Zurich / Neuroscience Center, University and ETH Zurich

Karin Grävare Silbernagel

Department of Physical Therapy, University of Delaware

Jess G. Snedeker (jess.snedeker@hest.ethz.ch)

University Hospital Balgrist, University of Zurich / Institute for Biomechanics, ETH Zurich

---

Research Article

Keywords: Mechanotransduction, tendon, calcium signaling, ion channels

Posted Date: November 10th, 2020

DOI: https://doi.org/10.21203/rs.3.rs-103392/v1

Abstract

Tendons enable movement by transferring muscle forces to the skeleton, and athletic performances critically rely on mechanically-optimized tendons. How load-bearing structures of tendon sense and adapt to physical demands is an open question of central importance to musculoskeletal medicine and human sports performance. Here, with calcium imaging in tendon explants and primary tendon cells we characterized how tenocytes detect mechanical forces and determined collagen fiber-sliding-induced shear stress as a key stimulus. CRISPR/Cas9 screening in human and rat tenocytes identified PIEZO1 as the crucial shear sensor. In rodents, elevated mechano-signaling increased tendon stiffness and strength both *in vitro* by pharmacological channel activation and *in vivo* by a *Piezo1* gain-of-function mutation. Strikingly, humans carrying the *PIEZO1* gain-of-function E756del mutation revealed a 16% average increase in normalized jumping height, with more effective storage of potential energy released during dynamic jumping maneuvers. We propose that PIEZO1-mediated mechano-signaling regulates tendon stiffness and impacts human athletic performance.

Introduction

Tendons connect muscle to bone and experience mechanical forces among the highest acting in the body (*1*). During movements with strong body acceleration, such as sprinting and jumping, tendons store and return energy in a catapult-like manner (*2*) and thereby enable the muscle-tendon unit to generate more power than is possible by the muscle alone (*3, 4*). Interestingly, regular high-load exercising increases the mechanical properties of tendons but with little to no change in tendon thickness (*5, 6*). This is confirmed by sprinters displaying tendons with elevated stiffness and strength compared to endurance runners and non-active individuals (*7*). Moreover, tendon diseases are conventionally treated with physical therapy that aims to restore the decreased stiffness and impaired performance by specific application of mechanical stimuli (*8, 9*). However, very little is known about acute cellular dynamics in response to physiological tendon loading and the underlying molecular mechanisms that regulate tendon stiffness.

Mechanotransduction is crucial to a wide variety of physiological processes, such as hearing, touch sensation, regulation of blood flow and pressure, as well as proprioception and breathing (*10-15*). These events rely on molecular mechanisms that convert mechanical forces into biological signals using various membrane proteins. In eukaryotes, several ion channels and receptors have been identified as mechanosensors (*16-24*). Among these, the mechanosensitive ion channel PIEZO1 is responsible for different mechanotransduction processes occurring in the lymphatic, cardiovascular, renal and skeletal systems (*25-30*). Genetic mutations in *PIEZO1* have revealed the physiological importance of this ion channel in humans. *PIEZO1* loss-of-function mutation leads to persistent congenital lymphoedema (*25, 26*), while a *PIEZO1* gain-of-function mutation that is common in individuals of African descent has been associated with malaria resistance (*31*). Although research on mechanically activated ion channels and receptors has made significant progress in recent years, the mechanosensors in tendons – one of the most mechanically challenged tissues of the human body – have not been identified.

We investigated tendon mechanotransduction by combining calcium (Ca^{2+}) imaging with simultaneous mechanical loading of tendon explants and isolated primary tendon cells. The physiological role of the identified molecular mechanism was then studied in mice and humans carrying gain-of-function mutations.

Results

Tenocytes sense tissue stretching by transient intracellular Ca^{2+} elevations.

To investigate how tendon cells (tenocytes) detect mechanical forces, we developed a functional imaging system that allows simultaneous fluorescence microscopy and tissue stretching of tendon explants from rat tails (Fig. 1a; see Methods for more details). Using this approach, we performed Ca^{2+} imaging in tissue-resident tenocytes labeled with Fluo-4. In an unstretched condition, we detected sparse spontaneous Ca^{2+} signals, however, upon stretching from 0-10% strain we observed a tissue-wide Ca^{2+} response (Fig. 1b and Movie S1). By testing different strain rates, we noticed distinct Ca^{2+} dynamics. While at low strain rate each tenocyte exhibited multiple Ca^{2+} signals, at high strain rate they displayed only a single Ca^{2+} response upon tendon stretching (Fig. 1c and S1). Additionally, with increasing strain rate higher tissue stretch was required to elicit a Ca^{2+} response in 50% of the cells (Fig. 1d). This strain rate dependency can partially be explained by a time lag between stimulus and Ca^{2+} signal of 0.77±0.18 s (Fig. 1e). We attributed the remaining differences to inherent viscoelastic properties of the tissue (Fig. S1e) and to potential cell-cell communication processes occurring predominately at low strain rate. The stretch-induced Ca^{2+} response was confirmed by two-photon fluorescence lifetime imaging (FLIM), with which we also determined absolute Ca^{2+} concentrations in tissue-resident tenocytes (Fig. S2) following OGB-1 loading (*32*). At rest, Ca^{2+} levels averaged 43±4 nM, however, upon tissue stretching Ca^{2+} levels increased by 18±6 nM reaching on average 61±8 nM (Fig. 1f and Movie S2). Similar Ca^{2+} elevations of 16±9 nM were detected in spontaneous signals, indicating that the stretch-induced Ca^{2+} responses were in a physiological range (Fig. 1g). Taken together, we observed a mechanosensitive calcium response in tenocytes that depends both on magnitude and rate of the tissue stretch.

Shear stress triggers calcium signals in isolated tenocytes.

During tissue stretching, collagen fibers – the load-bearing elements of the extracellular matrix – slide past each other (*33*). Tenocytes reside between these fibers and are therefore exposed to mechanical shear. Since fiber sliding is the predominant mechanism enabling the extension of tendon fascicles (*33*), we wondered whether shear stress could be the primary mechanical stimulus for tenocytes. We therefore quantified the fiber sliding by tracking cells from image sequences obtained at low strain rates and by comparing inter-fiber displacements (Fig. 2a). And by using a physical model we calculated the resulting shear stress, which ranged between 2 to 6 Pa depending on the cell height (Fig. 2b). Our analysis

suggests that shear stress levels may vary across cellular domains of tenocytes, likely being highest around narrow protrusions and lowest around the cell body. To test our prediction, we developed a microfluidic flow chamber that allows simultaneous Ca^{2+} imaging and shear stress stimulation of isolated primary tenocytes stained with Fluo-4 (Fig. 2c; see Methods for more details). Exposing tenocytes to a shear stress of 5 Pa, that occurs during tissue stretching, triggered a prominent Ca^{2+} response (Fig. 2d and Movie S3). The magnitude of shear stress stimulus determines the percentage of responsive cells (Fig. 2e) as well as the amplitude and duration of the Ca^{2+} response (Fig. S3). Interestingly, a Ca^{2+} response in about 50% of tenocytes is induced by a shear stress of 3.3 Pa, which falls well within the range of the calculated shear stress that occurs during tissue stretching (Fig. 2b). Together, this confirms the role of shear stress as a key mechanical stimulus for tenocytes, which show similar responsiveness across anatomical regions (Fig. 2f).

We noticed that Ca^{2+} signals typically start at the cell periphery both in isolated and in tissue-resident tenocytes (Fig. 2g). This is in line with our physical model which predicts that narrow regions (i.e. protrusions) experience the highest levels of shear stress.

PIEZO1 is required for the shear stress-induced response in tenocytes.

Since mechanotransduction relies on membrane proteins that convert mechanical stimuli into a biological signal (*34*), we wondered if shear stress in tenocytes activates mechanosensitive membrane channels mediating the Ca^{2+} influx. To test this, we performed mechanical stimulation in Ca^{2+}-free medium and observed no overt Ca^{2+} response in tissue-resident and isolated tenocytes (Fig. 3a). However, reperfusion with control medium containing Ca^{2+} restored the stimulus-evoked responses (Fig. 3a), suggesting a channel-mediated mechanism.

To identify the responsible ion channel, we focused on candidates associated with mechanosensitive cation channel characteristics that are highly expressed in both mouse tail tendons (*35*) and human Achilles tendons (*36*) (Fig. 3b). Using CRISPR/Cas9 genome editing, we generated efficient knockdowns of the selected genes in human primary tenocytes and tested their mechanosensitive response (Fig. 3c, d). Interestingly, from all examined knockdowns only cells depleted from PIEZO1, known as a shear sensor (*12, 16, 37*), showed a significant reduction in the shear stress response (Fig. 3e, f). This was further corroborated by analyzing additional CRISPR-guided RNAs targeting different regions of *PIEZO1* (Fig. 3g), thereby also precluding the contribution of potential off-target effects. Moreover, we obtained similar results with CRISPR/Cas9-mediated *Piezo1* knockdowns in rat tenocytes isolated from tail tendon fascicles (Fig. S4a-d). Taken together, this confirms that PIEZO1, an abundantly expressed ion channel in tendon tissues (Fig. S4e), is the crucial shear stress sensor in tenocytes.

PIEZO1 activity regulates the biomechanical properties of tendons.

To investigate the role of PIEZO1 in tendons, we performed *in vitro* and *in vivo* experiments. First, we confirmed that pharmacological activation of PIEZO1 by the specific agonist Yoda1 (*38*) triggers a robust Ca^{2+} response in tendon-resident tenocytes (Fig. S4f and Movie S4). Then, we wondered if recurrent pharmacological stimulation of tenocytes in cultured tendon fascicles could alter tissue stiffness. We therefore maintained tendon fascicles from rat tails in our custom bioreactor (*39*) with minimal loading to preserve tissue integrity (*39*) and stimulated tenocytes with 5 mM Yoda1 for 30 min every three days for two weeks (mimicking exercise) (Fig. 4a). To characterize changes in biomechanical properties over time, we cut each tendon fascicle in two, tested the first half at day 0 and the second half after the stimulation paradigm at day 16 (Fig. 4a). By comparing the ramp-to-failures of the two time-points, we noticed that stiffness and strength were significantly higher in Yoda1-stimulated fascicles relative to control fascicles (Fig. 4b). However, fascicle diameter was not affected (Fig. 3b). To verify if PIEZO1-mediated mechano-signaling regulates tendon stiffness *in vivo*, we analyzed tendons from mice carrying a *Piezo1* gain-of-function (*Piezo1*GOF) mutation equivalent to a human *PIEZO1* gain-of-function mutation (R2456H) (*31*). These mice express an overactive PIEZO1 that elicits stronger Ca^{2+} signals upon channel activation due to a longer inactivation time (*31*). Remarkably, ramp-to-failure experiments with plantaris tendons (foot flexor tendon) revealed an average increase in stiffness of 19% and in strength of 17% in *Piezo1*GOF mice compared to wild-type littermates, while the macroscale tendon morphology remained unchanged (Fig. 4c, d). These biomechanical differences are particularly prominent at high tendon loading and are very similar to reported changes in tendons of sprinters compared to endurance runners and non-active individuals (*7*). However, thorough analysis of collagen fibrils – the load-bearing microstructures (*33*) – from tendons of *Piezo1*GOF mice revealed no overt differences in fibril size distribution compared to their wild-type littermates (Fig. 4e-h). Hence, elevated mechano-signaling by PIEZO1 regulates tendon stiffness and strength without inducing a hypertrophic collagen production. Similarly, exercise-induced increases in tendon mechanical properties were not associated with changes in collagen fibril morphology (*40*). This likely indicates that increased tendon stiffness and strength in response to mechano-signaling may be induced by a denser collagen cross-linking (*41*).

PIEZO1 activity influences the jumping performance in humans.

Strong tendons are critical for high physical performance (*3*) and we wondered if our observed PIEZO1-mediated adaptations in tendon stiffness and strength could be relevant for human athletic performance. In fact, about one out of three individuals of African descent carries a *PIEZO1*GOF mutation known as E756del which has been associated with malaria resistance and represents the most abundant *PIEZO1*GOF mutation identified to date, particularly common in West African populations (*31*). Interestingly, athletes of West African descent (including African Americans) excel in sports performances related to sprinting and jumping (*42-44*), however, whether the E756del allele is overrepresented in elite athletes is unknown. But could human E756del carriers also present tendon adaptations that associate with athletic performance? We addressed this question in a double-blind study in which we investigated the Achilles tendon of 65 healthy African Americans and assessed their jumping performance.

Genotyping identified 20 heterozygous and two homozygous E756del carriers, and 43 non-carrier controls (Fig. 5a). We observed comparable demographics between E756del carriers and controls, with no differences in age, height, weight, physical activity or sports participation (Fig. 5b and S5). Ultrasound-based assessment of the Achilles tendon morphology showed no significant differences in tendon cross-sectional area and length between E756del carriers and controls (Fig. 5c, d), which is in line with the unchanged tendon morphology observed in *Piezo1*GOF mice (Fig. 4d-h). Since the tendon phenotype in *Piezo1*GOF mice was prominent at high degrees of tendon loading, we speculated that human E756del carriers may show athletic differences in exercises that evoke high tendon loading. We therefore measured the participant's maximal jumping performance in two related jumps, namely a countermovement jump (CMJ) and a drop countermovement jump (DCMJ) (Fig. 5e). The latter differs solely by an initial drop from a height of 20 cm, which leads to greater mechanical loads in the Achilles tendon (*45, 46*). Non-carrier controls demonstrated a similar performance in both jumps (Fig. 5f). Strikingly, E756del carriers performed significantly better in DCMJ, which evokes higher tendon loading, compared to CMJ (Fig. 5f). By normalizing the DCMJ-height to the CMJ-height, we assessed the impact of increased tendon loading on jumping performance and found an average performance of 111% in E756del carriers that significantly exceeded the average 95% reached by non-carriers (Fig. 5g). Hence, E756del carriers showed a net 16% average increase in normalized jumping performance compared to non-carriers, presumably because of a greater capacity of tendons to store and return elastic energy. Indeed, when converting the jump height into potential energy (i.e. mass x gravitational acceleration x jump height), we found that E756del carriers effectively stored and returned the drop energy (+8.1 J on average), whereas the controls did not (-2.1 J on average) (Fig. 5h). Accounting for the energy return of E756del carriers against the energy dissipation of controls, E756del carriers showed on average a significantly increased net energy return of 10.2 J. Thus, the E756del mutation likely influences sports performances that rely on the power output generated with high tendon loading, such as sprinting and jumping.

Discussion

In tendon mechanotransduction, it has been hypothesized that mechanical forces are converted into biological signals by mechanically activated membrane proteins (*47*). Isolated tenocytes are sensitive to pipette indentation (*48*) and show increased frequency of spontaneous calcium signals following a mechanical stimulation (*49*). However, evidence of acute responses to physiologically relevant mechanical stimuli and the underlying molecular sensing mechanisms have been elusive.

We developed a novel microscope-compatible functional imaging setup to enable direct observation of tenocytes during tissue stretching and harnessed it to characterize tendon mechanotransduction by Ca^{2+} imaging. We found a prompt calcium response in tenocytes upon tissue stretching and noticed that at low strain rate less stretch was required to elicit the response. This phenomenon might explain why physical rehabilitation strategies based on slowly performed resistance training show improved outcomes when treating tendinopathies (*50, 51*). Our data suggest that these improvements might arise

from an optimal compromise between maximizing cellular stimulation while minimizing tissue strains and loads.

Moreover, we identified shear stress as a key mechanical stimulus by determining the shear stress levels that occur during tissue stretching, applying them to isolated primary rat and human tendon cells and finding tight activation limits *in vitro* and *in situ*. By combining CRISPR/Cas9 screening with functional shear stress imaging, we found PIEZO1 as the crucial sensor driving shear stress-induced calcium signals.

To investigate the role of this ion channel in tendons, we analyzed the effect of elevated PIEZO1 mechano-signaling in tendons of rodents. *In vitro* pharmacological PIEZO1 stimulation and *in vivo* PIEZO1 overactivity both increased tendon stiffness and strength. Surprisingly, these changes seem not to result from a hypertrophic response. Instead, we suspect that a denser collagen cross-linking network causes the phenotypes. This would decrease the relative motions of collagen fibers and likely diminish the shear stress within the tissue, counteracting the elevated shear sensor signaling. Such tissue adaptation would imply a tenocyte mechanostat behavior (*52*), i.e. a feedback mechanism aiming to maintain optimal shear stress stimuli. An adapting cross-link network might also explain why exercise has very little to no effect on tissue- and fibril-morphology (*40*), and why the collagen matrix has a low turnover (*53*).

The high prevalence of the *PIEZO1*GOF E756del allele in the African population provides the opportunity to study the function of PIEZO1 in humans (*31*). The E756del mutation is particularly common in populations of West Africa, likely due to the potential protection it affords against malarial infection (*31*). Alongside with this potential role, our evidence suggests that the E756del mutation affects the human athletic performance. Specifically, E756del carriers perform significantly better than non-carriers in jumping maneuvers that include high degrees of tendon loading and of energy storage and return (*2, 45, 46*). This performance mechanism is presumably enhanced in tendons whose biomechanical characteristics are governed by an overactive PIEZO1, as we observed an increase in energy return in E756del carriers. While the performance is enabled by the muscle-tendon unit, it is worthy to note that skeletal muscle is likely not affected by the E756del mutation due to the very limited Piezo1 expression in muscle tissue (Fig. S4e) (*16*). The performance difference in humans as well as the tendon phenotype in mice both emerged at high degrees of tendon loading. Concurrently, both *Piezo1*GOF mice and E756del carriers displayed tendon morphology indistinguishable from wild-type controls. These findings strongly suggest that E756del carriers present a tendon phenotype similar to the one observed in *Piezo1*GOF mice.

The phenotypically improved power performance we identified in E756del carriers suggests that it might plausibly contribute to the fact that nearly all the top 500 sprint times of the men's 100 m are held by athletes of West African descent (including African Americans) (*43*), with these athletes reliably excelling in world-class sprinting competitions (*42*). However, whether the E756del allele is overrepresented in elite athletes is a tantalizing question that remains to be clarified.

Beyond implications for athletic performance, PIEZO1 may represent a therapeutic target in clinical indications for which physical rehabilitation is currently prescribed. Tendon pathologies are a common human condition, due to the high mechanical demands and the low intrinsic healing capacity (*1, 8*). They account for a substantial part of musculoskeletal diseases, which represent the second leading cause for years lived with disability worldwide (*8, 54, 55*). Pharmacological activation of PIEZO1 in diseased mechanically-inferior tendons might trigger tissue reinforcement and accelerate the healing process.

Methods

Calcium imaging of *ex vivo* tendon fascicles during stretching

Tendon fascicles were gently extracted from the tail of skeletally mature 14-18 week old female Wistar rats (approval by the Veterinary Office of the Canton of Zurich, ZH235/16). Rat tail tendon fascicles were stained with 5 µM Fluo-4 AM (Thermo Fisher Scientific F14217) for 2 h at 29° C and 3% O_2 in a modified Krebs-Henseleit solution (KHS) containing 126 mM NaCl, 3 mM KCl, 2 mM $CaCl_2$, 2 mM $MgSO_4$, 1.25 mM NaH_2PO_4, 26 mM $NaHCO_3$ and 10 mM glucose. Single tendon fascicles were subsequently mounted on a custom-designed tensile stretching device (equipped with two linear motors and a 20 N load cell) that was placed on the stage of an iMic widefield microscope (Thermo Fisher Scientific) (*56*). During stretching protocols, fascicles were continually perfused with KHS that was preheated to 29° C and steadily aerated by a gas mixture containing 95% N_2 and 5% CO_2 to maintain 3% O_2 and constant pH levels. Images were acquired with a 10x (N.A. 0.4) objective with excitation set at 488 nm wavelength and 100 ms exposure time. Prior to the stretching protocols, fascicles were preconditioned 5 times to 1.0% initial length L_0 (10mm mounting length from clamp-to-clamp). The cross-sectional area was measured at crimp disappearance and L_0 was defined at 1MPa tissue stress. Tissue strain was defined as $(L-L_0)/L_0$ in %, with sample length L. Tissue stress was calculated by dividing the force values through the cross-sectional area.

To investigate the cellular response to tissue stretching, single fascicles were stretched at three different strain rates (low 0.01% strain/s, medium 0.1% strain/s, high 1.0% strain/s) from 0 to 10% strain. Baseline activity was investigated at the preload of 1 MPa prior to initiating the stretching protocol. At medium and high strain rate, time lapses of one z-plane were recorded. At low strain rate, series of image stacks (50x2 µm) were acquired and subsequently deconvolved using Huygens Professional 18.10 (Scientific Volume Imaging) to quantify the micro-mechanical environment (at the cellular/collagen fiber level) needed to trigger intracellular calcium signals. To examine the time lag between the mechanical stimulus and the downstream calcium signals, tendon fascicles were subjected to one cycle of 2.7% strain at 30% strain/s.

Time lapse images were analyzed with the following steps. Cell movements were tracked with Imaris 7.7 (Bitplane AG, Switzerland) and the exported displacements were further used in a custom software (Matlab R2016a) that divided the images into 6x6 subimages and applied motion correction in each subimage. Calcium events were automatically detected and measured in the stabilized subimages using CHIPS (Cellular and Hemodynamic Image Processing Suite) (*57*). The interfiber sliding was calculated

from the relative displacements (in axial direction) of the cells on adjacent fibers (e.g. fiber u and v): , n and m are the respective cell numbers of the adjacent fibers, L_0 is the fiber length (*58*).

Fluorescence Lifetime Imaging (FLIM) of tendon fascicles

Isolated rat tail tendon fascicles were stained with 20 µM cell-permeable OGB-1 (Thermo Fisher Scientific O6806) for 2 h in KHS at 29° C and 3% O_2 and mounted on our tensile stretching device placed on the stage of a two-photon microscope and continually perfused with KHS during imaging. FLIM was performed on an upright Leica TCS SP8 FLIM two-photon microscope equipped with a tunable (680-1300 nm) 80 MHz infrared laser (Insight DS+ Dual from Spectra Physics) and four non-descanned FLIM enabled hybrid detectors. On the non-descanned detectors the following emission band pass filters were used: 460/50 nm, 525/50 nm, 585/40 nm, 650/50 nm. Data acquired from the channels 525/50 nm and 585/40 nm were used for the FLIM analysis. A 2.6 mm working distance Leica HC IRAPO 25x/1.0 water immersion objective was used for imaging. Time-correlated single-photon counting (TCSPC) was performed using a six channel Picoquant HydraHarp 400 together with the Picoquant Symphotime 64 software package. Femtosecond infrared laser pulses allowed for efficient two-photon fluorescence excitation and emission from a thin focal plane in the core of a tendon fascicle (ca. 30-100 µm deep in the tissue). A laser wavelength of 915 nm and a maximum laser power of 12.5 mW measured after the objective were used to avoid any signs of phototoxicity. To avoid photo-induced effects as well as statistical pile-up effects in the TCSPC histograms, the photon count rates on the detectors were always kept below 1% of the excitation rate. For fast sequential imaging an image size of 512 px in width and 80-110 px in height was used with a scanner frequency of 400 Hz.

The calcium calibration buffer kit from Thermo Fisher Scientific (C3008MP) was used in combination with the cell impermeable Ca^{2+} indicator OGB-1 at 1 µM to calibrate the [Ca^{2+}] readout (Fig. S2a). Temperature and pH were measured and considered by finely adjusting the estimated [Ca^{2+}] using Chris Patton's WEBMAXC program (http://web.stanford.edu/~cpatton/webmaxcS.htm) (*32*). The TCSPC histograms were fitted using a double-exponential tailfit within a time gate of 10ns using the Picoquant Symphotime software. From the tailfit, we calculated the amplitude weighted average lifetime, which was used throughout the study as a readout for [Ca^{2+}] using a suitable calibration function acquired from fitting a nonlinear Hill function to the OGB-1 calibration data (Fig. S2b).

To investigate baseline [Ca^{2+}] in tenocytes, tendon fascicles were imaged at the preload of 1 MPa after a preconditioning. Average image acquisition times were 120 s. A cellular compartment dependent region of interest analysis was performed to determine calcium concentrations in the cytoplasm and in the nucleus. The detected photons within the selected compartments were aggregated to obtain an overall [Ca^{2+}] estimate for that region. Ca^{2+} concentrations during calcium signals were examined with two different approaches. First, time-lapses were recorded after a stretch of the tendon fascicle to analyze the [Ca^{2+}] during spontaneous calcium signals. Second, time-lapses were acquired pre- and post-stretch to study the increase in [Ca^{2+}] induced by mechanical loading. In both cases, the stretching protocol

consisted of a single cycle to 2.7% strain at 1.0% strain/s starting and ending at the preload. The time-lapses were taken over a period of 15 min. To monitor the calcium signals, we maximized the temporal FLIM resolution while keeping an appropriate spatial resolution and the total number of collected photons. Therefore, we adjusted the acquisition rate to 0.066 Hz, which was sufficient to estimate the $[Ca^{2+}]$ during calcium events because of their average duration of around 27 s. The photons were aggregated within the selected single cell area. Subsequent data analysis calculated the $[Ca^{2+}]$ during calcium events. For illustration purposes, we applied a 2x2 px binning and a Gaussian filter ($\sigma = 3$) to the pixel maps of the $[Ca^{2+}]$-landscape. Data analysis and statistics, however, were performed using the raw data, not the filtered pixel maps.

Mathematical model for shear stress prediction in tenocytes

To predict the shear stress experienced by tenocytes during tissue stretching, we applied a numerical model that assumes cell heights (h) between 1-10 µm and that assumes individual tenocytes span the distance between two adjacent collagen fibers (*59*). Shear stress in tenocytes is generated by unilateral collagen fiber displacement, which leads to transverse displacement of the cell body. By definition, the shear stress (τ) arises through the application of a force (F) parallel to the cross-section over a certain surface (A) and is equal to the shear modulus (G) of the material multiplied by the shear strain (γ). The shear strain is defined as the transverse displacement (Δx) of the material divided by the initial height of the material (h) (Fig. 1i): . The shear modulus of a eukaryotic cell was previously estimated to be around G = 1.5 Pa (*60*) and the transverse material displacement (Δx) was calculated from the interfiber sliding (s) and the fiber length (l_{fiber} = 900 µm). This enables the estimation of shear stresses acting on tenocytes resulting from unilateral collagen fiber sliding.

Primary human and rat tenocyte cultures

Tendon cells were isolated either from fragments of human tendons (flexor hallucis longus, gracilis and semitendinosus) collected from female and male patients (between 24 and 58 years of age) undergoing treatment at the University Hospital Balgrist (permission 2015-0089 from the institutional review board of the Canton of Zurich and patient-informed consent) or from tail tendon fascicles of skeletally mature 14-18 week old female Wistar rats (approval by the Veterinary Office of the Canton of Zurich, ZH235/16). Next, tendon tissues were digested with 2mg/ml collagenase-D (Roche 11088866001) in Dulbecco's modified Eagle's medium (DMEM/F12 D8437) supplemented with 1% Amphotericin B (Gibco 15290-018) and 1% Penicillin-Streptomycin (Sigma-Aldrich P0781) for ca. 6 h at 37° C in a humidified atmosphere of 5% CO_2. Isolated cells were cultured on tissue culture plastic in DMEM/F12 with 10% heat inactivated fetal bovine serum (FBS, Gibco 10500) for 1-2 weeks and subsequently cryopreserved in liquid nitrogen until the start of the experiments.

Calcium imaging during application of shear stress on isolated tenocytes using flow chambers

Custom-made flow chambers were fabricated with the following procedure. A microscope slide was plasma treated, and 3 µl of polydimethylsiloxane (PDMS, Sylgard 184 Silicone Elastomer Kit, Dow Europe) was deposited in its center. Then a silanized PDMS stamp that was molded from the negative of the microgroove pattern (10 µm depth/ridge width/pitch) was placed on top. The assembly was subsequently cured at 70° C for 6 hours before detaching the stamps. PDMS microgrooves were chemically activated using two consecutive treatments of 0.1 mM N-sulfosuccinimidyl-6-(4'-azido-2'-nitrophenylamino) hexanoate (CovaChem 13414) in 50 mM 4-(2-hydroxyethyl)-1-piperazineethanesulfonic acid (Seraglob K 2101) under ultraviolet light for 10 min each. Substrates were then washed three times with sterile phosphate buffered saline (PBS) and coated with 50 µg/ml collagen-I (Corning 354249) in PBS overnight at 4°C, before being washed three times with deionized water and air dried (*61*). Finally, a block of PDMS containing a 0.4 mm high, 5 mm wide and 30 mm long canal was glued on top of the microscope slide, centering the microgrooved patch in the middle of the canal. A fine layer of PDMS containing additional 0.1% platinum-divinyltetramethyldisiloxane (abcr 146697) was used as glue and cured at 45° C for two hours.

Tenocytes were seeded in the flow chamber at a density of 38’000 cells/cm^2 and incubated at 29° C / 5% CO_2 / 3% O_2 overnight. Staining for 2 h with 1 µM Fluo 4-AM diluted in KHS containing 0.02% pluronic F-127 was performed before placing the flow chamber on the microscope stage and connecting it to a syringe pump (Cetoni, low-pressure module). Next, the flow chambers were flushed for a few minutes at a flow rate of 0.1 ml/min (resulting in negligible shear stress of ca. 0.01 Pa) with KHC that was preheated to 29° C and degassed to 3% O_2 using a gas mixer. Appropriate flow rates resulting in specific shear stresses on the cell substrate were calculated using established formulas of fluid flow in rectangular channels (*62*). During shear stress experiments, image stacks (5x3 µm) were acquired with the iMic widefield microscope (10x objective) at a frequency of 1 Hz, a wavelength of 488 nm, and an exposure time of 100 ms.

Image analysis was done with an initial average intensity Z-projection of the image stacks, followed by a segmentation of individual cell bodies performed with a custom ImageJ script based on the fluorescence at the baseline, i.e. 30 s interval before application of the shear stress stimulus. The mean fluorescence intensity of each segmented cell was normalized to the average intensity measured at the baseline. A calcium signal in a cell was defined as such when the normalized fluorescence intensity ($\Delta F/F_0$) exceeded the baseline fluorescence intensity by 10 times the standard deviation of the baseline during a 20 s interval following shear stress exposure.

Generation of CRISPR/Cas9-mediated knockdown cells

Single guide RNAs (sgRNAs) against multiple candidate genes were designed with the CRISPRdirect online tool http://crispr.dbcls.jp (*63*). Only highly specific target sites were selected, the respective sequences are listed in Table S1. A non-targeting control sgRNA was chosen from the study of Morgens et al. (*64*) and checked for low targeting potential by BLASTN 2.8.0 search. Target sequences oligos were synthesized with BsmBI restriction site overhangs by Microsynth (Balgach, Switzerland) and then

annealed and cloned into the lentiCRISPRv2 transfer plasmid, a gift from Feng Zhang (Addgene plasmid #52961; (*65*)), following the provided protocol of the Feng Zhang Lab.

Lentiviral particles were produced by co-transfection of the lentiCRISPRv2 plasmid, containing the respective gRNA-sequence, with the packaging plasmids pCMV-VSV-G (a gift from Bob Weinberg; Addgene plasmid #8454; (*66*)) and psPAX2 (a gift from Didier Trono; Addgene plasmid #12260) into HEK293T cells using Lipofectamine 3000 (Thermo Fisher Scientific L3000008) and following the manufacturer's instructions.

For transduction, human and rat tenocytes were incubated for 24 h with supernatant containing the viral particles and supplemented with 8 µg/ml Polybrene. Subsequently, human and rat cells were selected with 3 µg/ml Puromycin (Gibco A1113803) for 3 days or with 4 µg/ml for 7 days, respectively. The efficiency of the knockouts was tested with quantitative real-time PCR, immunofluorescence and western blotting.

RNA isolation from tissues and cells and quantitative real-time PCR

Freshly isolated tissues were snap frozen in liquid nitrogen and subsequently homogenized with QIAzol lysis reagent (Qiagen 79306) using a cryogenic grinder (SPEXSamplePrep FreezerMill 6870). 1-bromo-3-chloropropane (Sigma-Aldrich B9673) was added to the tissue lysates at a 1:4 ratio, and the RNA containing aqueous phase was obtained using Phase Lock Gel - Heavy (LabForce 2302830). *In vitro* tenocytes were lysed with RLT/bME buffer. Subsequently, RNA from tissue and cell lysates was extracted using the RNeasy micro Kit (Qiagen 74004) following the protocol provided by the manufacturer. Quality and quantity of the RNA was measured with a NanoDrop 1000 Spectrophotometer (Thermo Fisher Scientific).

cDNA was synthesized from 500 ng of total RNA using a High-Capacity cDNA Reverse Transcription Kit with RNAse Inhibitor according to the manufacturer instructions (Applied Biosystems 4374966). Gene expression analysis was performed by quantitative real-time PCR with cDNA corresponding to 10 ng of starting RNA using the PowerUp SYBR Green Master Mix (Thermo Fisher Scientific A25742). The samples were amplified using a StepOnePlus Real-Time PCR System (Applied Biosystems) with the following conditions: 95° C for 10 min followed by 40 PCR cycles of 95° for 15 s and 60° C for 1 min. All experiments were run with technical triplicates. Relative gene expression levels were quantified using the 2^{-ddCT} method with either ANXA5 or GAPDH as reference gene. All primers are listed in Table S2.

Immunofluorescence

Cells seeded in flow chambers were fixed with 4% formaldehyde in PBS (Carl Roth 3105.2) for 20 min at room temperature and subsequently permeabilized with 0.1% Triton-X (Axonlab 10029070) and 0.5% bovine albumin serum (BSA, VWR P6154) in PBS for 10 min. Samples were incubated with specific primary antibodies in PBS with 3% BSA for 1 h and afterwards with a secondary fluorescently-labeled antibody. Between every step samples were washed three times with PBS. Primary antibodies were used

against PIEZO1 (Novus Biologicals NBP1-78446 for human cells, 1:25; Alomone Labs APC-087 for rat cells, 1:300). Actin filaments were stained with Alexa Fluor 568 phalloidin (Thermo Fisher Scientific A12380, 1:200) and cell nuclei with NucBlue (Thermo Fisher Scientific R37605). Alexa Fluor 488 conjugated donkey anti-rabbit (Thermo Fisher Scientific A-21206, 1:100) was used as a secondary antibody. Immunofluorescence images were acquired with the iMic spinning disk confocal microscope using an oil-immersion 60x (N.A. 1.35) objective.

Western blotting

Cells were washed with PBS and lysed directly in the cell culture dish with 80 µl of 1x reduced Laemmli buffer (Fisher Scientific 15493939) and boiled for 5 min at 95°C. 15 µl of each sample was loaded onto a 4-15% Mini-PROTEAN TGX stain-free protein gel (Bio-Rad 4568086). Total protein was analyzed using the Criterion Stain-free imaging system (Bio-Rad) and subsequently transferred on polyvinylidene difluoride membranes using the Trans-Blot-Turbo Transfer System (Bio-Rad). Membrane blocking was carried out with 5% nonfat dry milk/TBS-T for 1 h at room temperature. The primary antibodies targeting PIEZO1 (Thermo Fisher Scientific MA5-32876, 1:500) and β-tubulin (MERCK Millipore MAB3408, 1:10’000) were diluted in 5% BSA/TBS-T and incubated overnight at 4° C. Next, the membranes were washed 3 times in TBS-T and incubated with the secondary antibody (anti-mouse, Sigma-Aldrich SAB3701073, 1:20’000) for 1 h at room temperature. Images were taken using UltraScence Pico Ultra Western Substrate (GeneDireX CCH345-B) and the ChemiDoc MP imaging system (Bio-Rad).

Tendon explants cultured in bioreactor and subjected to sham or Yoda1 stimulation

Rat tail tendon fascicles were freshly isolated and placed into culture medium (high glucose Dulbecco’s Modified Eagle’s Medium, Sigma Aldrich D6429, supplemented with 1% Penn/Strep, 200 µM ascorbic acid, Wako Chemicals 013-19641, and 1% N-2 supplement, Thermo Fisher Scientific 7001585). Each fascicle was cut in half, one half was used for mechanical testing at day 0, while the other half was cultured in our custom-made bioreactor at the preload (crimp disappearance, i.e. minimal mechanical load) and mechanically tested at day 16 (*39*). Distal and proximal samples were randomly distributed between the two days. Diameters were measured at day 0 and day 16 using a 10x objective (Motic AE2000). Cultured fascicles underwent either sham or 5 µM Yoda1 stimulations for 30 min on days 0, 3, 6, 9 and 12 post-isolation. Following the 30 min treatment, fascicles were washed once with medium, then resuspended in medium and incubated at 29° C, 5% CO_2 and 3% O_2. Ramp-to-failure experiments were performed to assess the biomechanical properties. Samples were preloaded to 0.04 N and preconditioned 5 times to 1% strain. Subsequently, a ramp-to-failure was carried out at 1% strain/s. Fascicle stiffness was calculated in the linear region of the force-strain curves and fascicle strength was determined from the maximal force.

Biomechanical testing and analysis

The biomechanical properties of plantaris tendons from wild-type and *Piezo1*GOF mice (*31*) were investigated with ramp-to-failure experiments. Age-matched littermates (20-21 weeks old) were

euthanized and stored at -80° C until the day of experiment (approval by the Institutional Animal Care and Use Committees of Scripps Research in accordance with the guidelines established by the Association for Assessment and Accreditation of Laboratory Animal Care International (AAALAC)). After thawing, plantaris tendons were carefully isolated and tested in uniaxial tension using a custom clamping technique on a universal testing machine that recorded force-displacement data (Zwick Z010 TN, 20 N load-cell) (*67*). During testing, tendons were kept in a custom chamber filled with KHS, preloaded to 0.1 N (initial length L_0 corresponding to 0% strain) and preconditioned 5 times to 1% strain (preload reapplied after every cycle). Subsequently, samples were ramped to failure at a constant strain-rate of 1% strain/s. The diameter was measured in microscopic images of the plantaris tendons (4x objective, Motic AE2000). Tendon stiffness was calculated in the linear region of the force-strain curves and tendon strength was determined from the maximal force.

Transmission electron microscopy

Plantaris tendons were freshly isolated from age-matched littermates (29-34 weeks old) euthanized in the middle of the day (normal light/dark cycle) and sequentially fixed with 2.5% glutaraldehyde (Sigma-Aldrich G5882) in 0.1 M sodium cacodylate buffer (pH 7.2), with 1% OsO_4 in 0.1 M sodium cacodylate buffer at room temperature and with 1% uranyl acetate in H_2O at room temperature for at least 1 hour per step. Samples were rinsed 3 times between the fixation steps and finally with H_2O prior to dehydration in an ethanol series and embedding in Epon. Ultrathin (70 nm) sections were post-stained with Reynolds lead citrate and imaged in a FEI Talos 120 at 120 kV using a bottom mounted Ceta camera (CMOS, 4k x 4k pixels) using MAPS software (Thermo Fisher Scientific). Segmentation of the cross-sectional area of collagen fibrils was performed with the Trainable Weka Segmentation Fiji plugin (*68*).

Participants of the human study - activity level and sports participation

Healthy self-reported African American participants (at least 18 years old) were enrolled after approval by the Institutional Review Board of the University of Delaware (ID-1420251-3) and written informed consent. A clinical evaluation with ultrasound imaging was carried out to ensure that the subjects had no underlying pathologies in their Achilles tendons. Additionally, the Victorian Institute for Sports Assessment - Achilles questionnaire (VISA-A) was applied to confirm that the Achilles tendons were healthy (*69*). Participants reported their highest level of sports participation (recreational, secondary school, collegiate or professional) and their history of sports participation. The Physical Activity Scale (PAS) was used to assess the subject's reported current physical activity level (*70*).

Ultrasound-based assessment of the human Achilles tendon morphology

B-mode ultrasound imaging (LOGIQ *e* ultrasound system (GE Healthcare, USA) with wide-band linear array probe (5.0-13.0 MHz)) was used to analyze the Achilles tendon morphology Briefly, Achilles tendon thickness and cross-sectional area were measured at a distance of 2.5 cm from the calcaneal osteotendinous junction (axial direction) in the images acquired parallel and perpendicular to the fiber orientation (each 3 repetitions), respectively (*71*). Achilles tendon length was measured as the distance

from the calcaneal osteotendinous junction to the myotendinous junction of the gastrocnemius and soleus muscles using extended field of view (*71*). The software OsiriX MD (Pixmeo SARL, Switzerland) was used to analyze the ultrasound images.

Functional performance tests

To investigate the jump heights, we used the MuscleLabÔ (Ergotest Innovation, Norway) light mat measurement system, which creates an infrared light field 4 mm above the floor and records beam interruptions. Participant height and weight were recorded prior to jumping tests. Jump height was calculated by MuscleLabÔ using participant weight, ground contact time, and flight time. Participants performed two different jump tests. In each test the participants were asked to place their hands behind their back and to jump as high as possible. The first test was a single leg countermovement jump (CMJ) in which the participants started by standing on the floor on one leg then quickly bent the knee before jumping straight up as high as possible (*72*). This was repeated three times with each leg. The second test was a single leg drop countermovement jump (DCMJ), in which participants jumped off of a 20 cm high box and then jumped vertically as high as possible (*72*). For each leg, the average height of three trials was used for analysis.

Genotyping of the human *PIEZO1*GOF (E756del) mutation

Saliva samples were collected using Oragene DNA collection kits (OG-500, DNA Genotek). Genomic DNA isolation was performed according to the manufacturer instructions using the prepIT-L2P reagent (PT-L2P, DNA Genotek) included in the kit. The region containing the E756 locus was amplified with PCR (forward primer 5’ CAGGCAGGATGCAGTGAGTG 3’ and reverse primer 5’ GGACATGGCACAGCAGACTG 3’) (*31*). This amplicon (ca. 200 bp) was sequenced using both primers to identify non-carriers and E756del carriers.

Statistical analysis

For multiple-comparisons, data were analyzed with one-way ANOVA (Tukey’s or Dunnett’s test). Inter-group comparisons were performed with two-tailed Student’s t test or two-tailed Mann-Whitney test. For mouse and human data, n = number of animals or participants, at least n = 4 was used. Analyses using linear mixed effects models (lme4 package in R) were conducted for the biomechanical experiments with mouse tendons (mouse ID as random effect and litter as fixed effect, Bonferroni-Holm correction) and for the human jumping data (subject ID as random effect and leg as fixed effect). Age, height, weight, highest level of sports participation and activity level of the participants were tested as covariates. Significance levels were set as $*p < 0.05$, $**p < 0.01$, $***p < 0.001$. In the figures, data are represented as means ± SEM. Analyses performed with GraphPad Prism 8.2 or RStudio v1.1.383.

References

1. S. P. Magnusson, H. Langberg, M. Kjaer, The pathogenesis of tendinopathy: balancing the response to loading. *Nat Rev Rheumatol* **6**, 262-268 (2010).
2. M. H. Dickinson *et al.*, How animals move: an integrative view. *Science* **288**, 100-106 (2000).
3. T. J. Roberts, R. L. Marsh, P. G. Weyand, C. R. Taylor, Muscular force in running turkeys: the economy of minimizing work. *Science* **275**, 1113-1115 (1997).
4. A. M. Wilson, J. C. Watson, G. A. Lichtwark, Biomechanics: A catapult action for rapid limb protraction. *Nature* **421**, 35-36 (2003).
5. A. Arampatzis, K. Karamanidis, K. Albracht, Adaptational responses of the human Achilles tendon by modulation of the applied cyclic strain magnitude. *J Exp Biol* **210**, 2743-2753 (2007).
6. K. M. Heinemeier *et al.*, Uphill running improves rat Achilles tendon tissue mechanical properties and alters gene expression without inducing pathological changes. *J Appl Physiol (1985)* **113**, 827-836 (2012).
7. A. Arampatzis, K. Karamanidis, G. Morey-Klapsing, G. De Monte, S. Stafilidis, Mechanical properties of the triceps surae tendon and aponeurosis in relation to intensity of sport activity. *J Biomech* **40**, 1946-1952 (2007).
8. G. Riley, Tendinopathy--from basic science to treatment. *Nat Clin Pract Rheumatol* **4**, 82-89 (2008).
9. G. Nourissat, F. Berenbaum, D. Duprez, Tendon injury: from biology to tendon repair. *Nat Rev Rheumatol* **11**, 223-233 (2015).
10. B. Pan *et al.*, TMC1 Forms the Pore of Mechanosensory Transduction Channels in Vertebrate Inner Ear Hair Cells. *Neuron* **99**, 736-753 e736 (2018).
11. S. S. Ranade *et al.*, Piezo2 is the major transducer of mechanical forces for touch sensation in mice. *Nature* **516**, 121-125 (2014).
12. J. Li *et al.*, Piezo1 integration of vascular architecture with physiological force. *Nature* **515**, 279-282 (2014).
13. S. Wang *et al.*, Endothelial cation channel PIEZO1 controls blood pressure by mediating flow-induced ATP release. *J Clin Invest* **126**, 4527-4536 (2016).
14. S. H. Woo *et al.*, Piezo2 is the principal mechanotransduction channel for proprioception. *Nat Neurosci* **18**, 1756-1762 (2015).
15. K. Nonomura *et al.*, Piezo2 senses airway stretch and mediates lung inflation-induced apnoea. *Nature* **541**, 176-181 (2017).
16. B. Coste *et al.*, Piezo1 and Piezo2 are essential components of distinct mechanically activated cation channels. *Science* **330**, 55-60 (2010).
17. L. Kang, J. Gao, W. R. Schafer, Z. Xie, X. S. Xu, C. elegans TRP family protein TRP-4 is a pore-forming subunit of a native mechanotransduction channel. *Neuron* **67**, 381-391 (2010).
18. M. R. Servin-Vences, M. Moroni, G. R. Lewin, K. Poole, Direct measurement of TRPV4 and PIEZO1 activity reveals multiple mechanotransduction pathways in chondrocytes. *Elife* **6**, (2017).

19. A. J. Patel *et al.*, A mammalian two pore domain mechano-gated S-like K+ channel. *EMBO J* **17**, 4283-4290 (1998).
20. F. Maingret, M. Fosset, F. Lesage, M. Lazdunski, E. Honoré, TRAAK is a mammalian neuronal mechano-gated K+ channel. *J Biol Chem* **274**, 1381-1387 (1999).
21. J. Xu *et al.*, GPR68 Senses Flow and Is Essential for Vascular Physiology. *Cell* **173**, 762-775 e716 (2018).
22. R. O'Hagan, M. Chalfie, M. B. Goodman, The MEC-4 DEG/ENaC channel of Caenorhabditis elegans touch receptor neurons transduces mechanical signals. *Nat Neurosci* **8**, 43-50 (2005).
23. M. Zhang *et al.*, Structure of the mechanosensitive OSCA channels. *Nat Struct Mol Biol* **25**, 850-858 (2018).
24. S. E. Murthy *et al.*, OSCA/TMEM63 are an Evolutionarily Conserved Family of Mechanically Activated Ion Channels. *Elife* **7**, (2018).
25. V. Lukacs *et al.*, Impaired PIEZO1 function in patients with a novel autosomal recessive congenital lymphatic dysplasia. *Nat Commun* **6**, 8329 (2015).
26. E. Fotiou *et al.*, Novel mutations in PIEZO1 cause an autosomal recessive generalized lymphatic dysplasia with non-immune hydrops fetalis. *Nat Commun* **6**, 8085 (2015).
27. K. Retailleau *et al.*, Piezo1 in Smooth Muscle Cells Is Involved in Hypertension-Dependent Arterial Remodeling. *Cell Rep* **13**, 1161-1171 (2015).
28. R. Peyronnet *et al.*, Piezo1-dependent stretch-activated channels are inhibited by Polycystin-2 in renal tubular epithelial cells. *EMBO Rep* **14**, 1143-1148 (2013).
29. S. M. Cahalan *et al.*, Piezo1 links mechanical forces to red blood cell volume. *Elife* **4**, (2015).
30. W. Sun *et al.*, The mechanosensitive Piezo1 channel is required for bone formation. *Elife* **8**, (2019).
31. S. Ma *et al.*, Common PIEZO1 Allele in African Populations Causes RBC Dehydration and Attenuates Plasmodium Infection. *Cell* **173**, 443-455 e412 (2018).
32. K. Zheng *et al.*, Time-Resolved Imaging Reveals Heterogeneous Landscapes of Nanomolar Ca(2+) in Neurons and Astroglia. *Neuron* **88**, 277-288 (2015).
33. H. R. Screen, D. A. Lee, D. L. Bader, J. C. Shelton, An investigation into the effects of the hierarchical structure of tendon fascicles on micromechanical properties. *Proc Inst Mech Eng H* **218**, 109-119 (2004).
34. S. E. Murthy, A. E. Dubin, A. Patapoutian, Piezos thrive under pressure: mechanically activated ion channels in health and disease. *Nat Rev Mol Cell Biol* **18**, 771-783 (2017).
35. S. L. Wunderli *et al.*, Tendon response to matrix unloading is determined by the patho-physiological niche. *Matrix Biol*, (2020).
36. M. J. Peffers *et al.*, Transcriptome analysis of ageing in uninjured human Achilles tendon. *Arthritis Res Ther* **17**, 33 (2015).
37. S. S. Ranade *et al.*, Piezo1, a mechanically activated ion channel, is required for vascular development in mice. *Proc Natl Acad Sci U S A* **111**, 10347-10352 (2014).

38. R. Syeda *et al.*, Chemical activation of the mechanotransduction channel Piezo1. *Elife* **4**, (2015).
39. S. L. Wunderli *et al.*, Minimal mechanical load and tissue culture conditions preserve native cell phenotype and morphology in tendon-a novel ex vivo mouse explant model. *Journal of orthopaedic research : official publication of the Orthopaedic Research Society* **36**, 1383-1390 (2018).
40. S. P. Magnusson, M. Kjaer, The impact of loading, unloading, ageing and injury on the human tendon. *J Physiol* **597**, 1283-1298 (2019).
41. C. T. Thorpe, R. J. Stark, A. E. Goodship, H. L. Birch, Mechanical properties of the equine superficial digital flexor tendon relate to specific collagen cross-link levels. *Equine Vet J Suppl*, 538-543 (2010).
42. Olympic Games, 100m men. *www.olympic.org/athletics/100m-men*, (Accessed May 2020).
43. World Athletics, 100 meters men. *www.worldathletics.org/records/all-time-toplists/sprints/100-metres/outdoor/men/senior*, (Accessed May 2020).
44. World Athletics, Long jump men. *www.worldathletics.org/records/all-time-toplists/jumps/long-jump/outdoor/men/senior*, (Accessed May 2020).
45. M. Ishikawa, E. Niemela, P. V. Komi, Interaction between fascicle and tendinous tissues in short-contact stretch-shortening cycle exercise with varying eccentric intensities. *J Appl Physiol (1985)* **99**, 217-223 (2005).
46. J. E. Earp *et al.*, Influence of muscle-tendon unit structure on rate of force development during the squat, countermovement, and drop jumps. *J Strength Cond Res* **25**, 340-347 (2011).
47. M. Lavagnino *et al.*, Tendon mechanobiology: Current knowledge and future research opportunities. *Journal of orthopaedic research : official publication of the Orthopaedic Research Society* **33**, 813-822 (2015).
48. M. E. Wall, A. J. Banes, Early responses to mechanical load in tendon: role for calcium signaling, gap junctions and intercellular communication. *J Musculoskelet Neuronal Interact* **5**, 70-84 (2005).
49. E. Maeda, Y. Hagiwara, J. H. Wang, T. Ohashi, A new experimental system for simultaneous application of cyclic tensile strain and fluid shear stress to tenocytes in vitro. *Biomed Microdevices* **15**, 1067-1075 (2013).
50. M. Kongsgaard *et al.*, Corticosteroid injections, eccentric decline squat training and heavy slow resistance training in patellar tendinopathy. *Scand J Med Sci Sports* **19**, 790-802 (2009).
51. R. Beyer *et al.*, Heavy Slow Resistance Versus Eccentric Training as Treatment for Achilles Tendinopathy: A Randomized Controlled Trial. *Am J Sports Med* **43**, 1704-1711 (2015).
52. H. M. Frost, Bone “mass” and the “mechanostat”: a proposal. *The anatomical record* **219**, 1-9 (1987).
53. K. M. Heinemeier, P. Schjerling, J. Heinemeier, S. P. Magnusson, M. Kjaer, Lack of tissue renewal in human adult Achilles tendon is revealed by nuclear bomb (14)C. *FASEB J* **27**, 2074-2079 (2013).
54. M. S. Forde, L. Punnett, D. H. Wegman, Prevalence of musculoskeletal disorders in union ironworkers. *J Occup Environ Hyg* **2**, 203-212 (2005).
55. E. Sebbag *et al.*, The world-wide burden of musculoskeletal diseases: a systematic analysis of the World Health Organization Burden of Diseases Database. *Ann Rheum Dis* **78**, 844-848 (2019).

56. A. Gautieri *et al.*, Advanced glycation end-products: Mechanics of aged collagen from molecule to tissue. *Matrix Biol* **59**, 95-108 (2017).
57. M. J. P. Barrett, K. D. Ferrari, J. L. Stobart, M. Holub, B. Weber, CHIPS: an Extensible Toolbox for Cellular and Hemodynamic Two-Photon Image Analysis. *Neuroinformatics* **16**, 145-147 (2018).
58. Y. Li, G. Fessel, M. Georgiadis, J. G. Snedeker, Advanced glycation end-products diminish tendon collagen fiber sliding. *Matrix Biol* **32**, 169-177 (2013).
59. C. M. McNeilly, A. J. Banes, M. Benjamin, J. R. Ralphs, Tendon cells in vivo form a three dimensional network of cell processes linked by gap junctions. *J Anat* **189 (Pt 3)**, 593-600 (1996).
60. M. J. Song *et al.*, Mapping the mechanome of live stem cells using a novel method to measure local strain fields in situ at the fluid-cell interface. *Plos One* **7**, e43601 (2012).
61. T. Razafiarison, U. Silvan, D. Meier, J. G. Snedeker, Surface-Driven Collagen Self-Assembly Affects Early Osteogenic Stem Cell Signaling. *Adv Healthc Mater* **5**, 1481-1492 (2016).
62. R. Cornish, Flow in a pipe of rectangular cross-section. *Proceedings of the Royal Society of London. Series A, Containing Papers of a Mathematical and Physical Character* **120**, 691-700 (1928).
63. Y. Naito, K. Hino, H. Bono, K. Ui-Tei, CRISPRdirect: software for designing CRISPR/Cas guide RNA with reduced off-target sites. *Bioinformatics* **31**, 1120-1123 (2015).
64. D. W. Morgens *et al.*, Genome-scale measurement of off-target activity using Cas9 toxicity in high-throughput screens. *Nature communications* **8**, 15178 (2017).
65. N. E. Sanjana, O. Shalem, F. Zhang, Improved vectors and genome-wide libraries for CRISPR screening. *Nat Methods* **11**, 783-784 (2014).
66. S. A. Stewart *et al.*, Lentivirus-delivered stable gene silencing by RNAi in primary cells. *RNA* **9**, 493-501 (2003).
67. G. Fessel *et al.*, Advanced glycation end-products reduce collagen molecular sliding to affect collagen fibril damage mechanisms but not stiffness. *Plos One* **9**, e110948 (2014).
68. I. Arganda-Carreras *et al.*, Trainable Weka Segmentation: a machine learning tool for microscopy pixel classification. *Bioinformatics* **33**, 2424-2426 (2017).
69. J. M. Robinson *et al.*, The VISA-A questionnaire: a valid and reliable index of the clinical severity of Achilles tendinopathy. *Br J Sports Med* **35**, 335-341 (2001).
70. G. Grimby, Physical activity and muscle training in the elderly. *Acta Med Scand Suppl* **711**, 233-237 (1986).
71. K. G. Silbernagel, K. Shelley, S. Powell, S. Varrecchia, Extended field of view ultrasound imaging to evaluate Achilles tendon length and thickness: a reliability and validity study. *Muscles Ligaments Tendons J* **6**, 104-110 (2016).
72. K. G. Silbernagel, A. Gustavsson, R. Thomee, J. Karlsson, Evaluation of lower leg function in patients with Achilles tendinopathy. *Knee Surg Sports Traumatol Arthrosc* **14**, 1207-1217 (2006).

Declarations

Acknowledgments: We thank Barbara Niederöst for technical support; Andreas Ziegler, Beda Rutishauser and Elias Bachmann for engineering assistance; Lilian Gasser (Statistical Consulting Group, ETH Zurich) for statistical support and members of the Snedeker group for constructive discussions. We further thank Dr. Ardem Patapoutian for providing Piezo1GOF mice and valuable feedback. We acknowledge the help of Ursula Lüthi and Dr. Andres Käch from the Center for Microscopy and Image Analysis (University of Zurich) in TEM microscopy. **Funding:** Was provided by the Swiss National Science Foundation, grants number 165670 and 185095.

Author contributions: F.S.P., P.C.J., A.S.S. and J.G.S. designed experiments and wrote the manuscript. F.S.P. performed calcium imaging of tendon explants. F.S.P., K.D.F., D.H., S.C., A.N.H., U.S. and B.W designed and analyzed the calcium imaging experiments. P.C.J. and F.S.P. carried out and analyzed the calcium imaging experiments with shear stress stimulation of cells. M.J.A., F.S.P., M.B. and B.P.T. generated and analyzed knockout cells. S.F.F., M.B. and U.B. helped with human tendon tissues and isolation of primary cells. F.S.P. and S.M. performed mice experiments. S.H., K.G.S., F.S.P. and J.G.S. designed and performed the human study. F.S.P. and B.P.T. carried out human genotyping. F.S.P., S.H. and T.G. analyzed the human data.

Competing interests: Authors declare no competing interests.

Data and code availability: The data relating to the findings of this study, the stretching-device software and Matlab, ImageJ and R codes are available from the corresponding author upon request. The toolbox CHIPS is freely available (*29*).

Figures

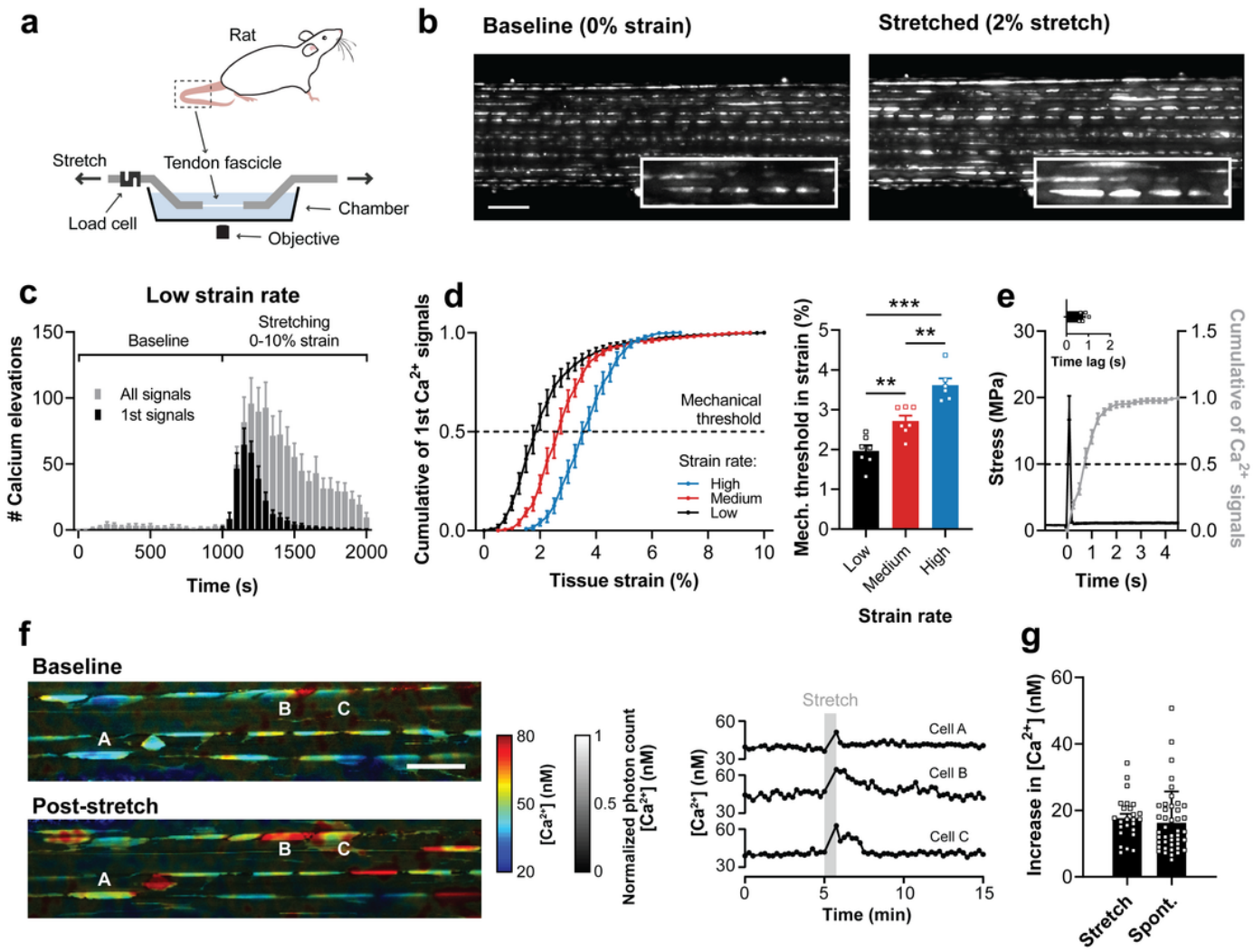

Figure 1

Mechanically-induced Ca2+ elevations in tissue-resident tenocytes. Schematic of setup (a) used for simultaneous stretching and Ca2+ imaging (b) of tendon fascicles from rat tails (scale bar, 100 µm). (c) Stretching induces Ca2+ elevations (n=7 fascicles). (d) Cumulative of first Ca2+ signals shows a right-shift with increasing strain rate, mechanical threshold at 1.96±0.35% strain for low (0.01% strain/s, n=7 fascicles), at 2.72±0.33% strain for medium (0.1% strain/s, n=7 fascicles) and at 3.62±0.38% strain for high (1.0% strain/s, n=6 fascicles), one-way ANOVA with multiple comparisons (Tukey's test). (e) Time lag between mechanical stimulus and Ca2+ elevation (n=5 fascicles). (f) FLIM acquired [Ca2+] landscapes of fascicles (scale bar, 50 µm) reveal (g) significant [Ca2+] increases upon stretching (n=25 cells from 6 fascicles) and during spontaneous Ca2+ signals (n=43 cells from 13 fascicles), paired Student's t-test.

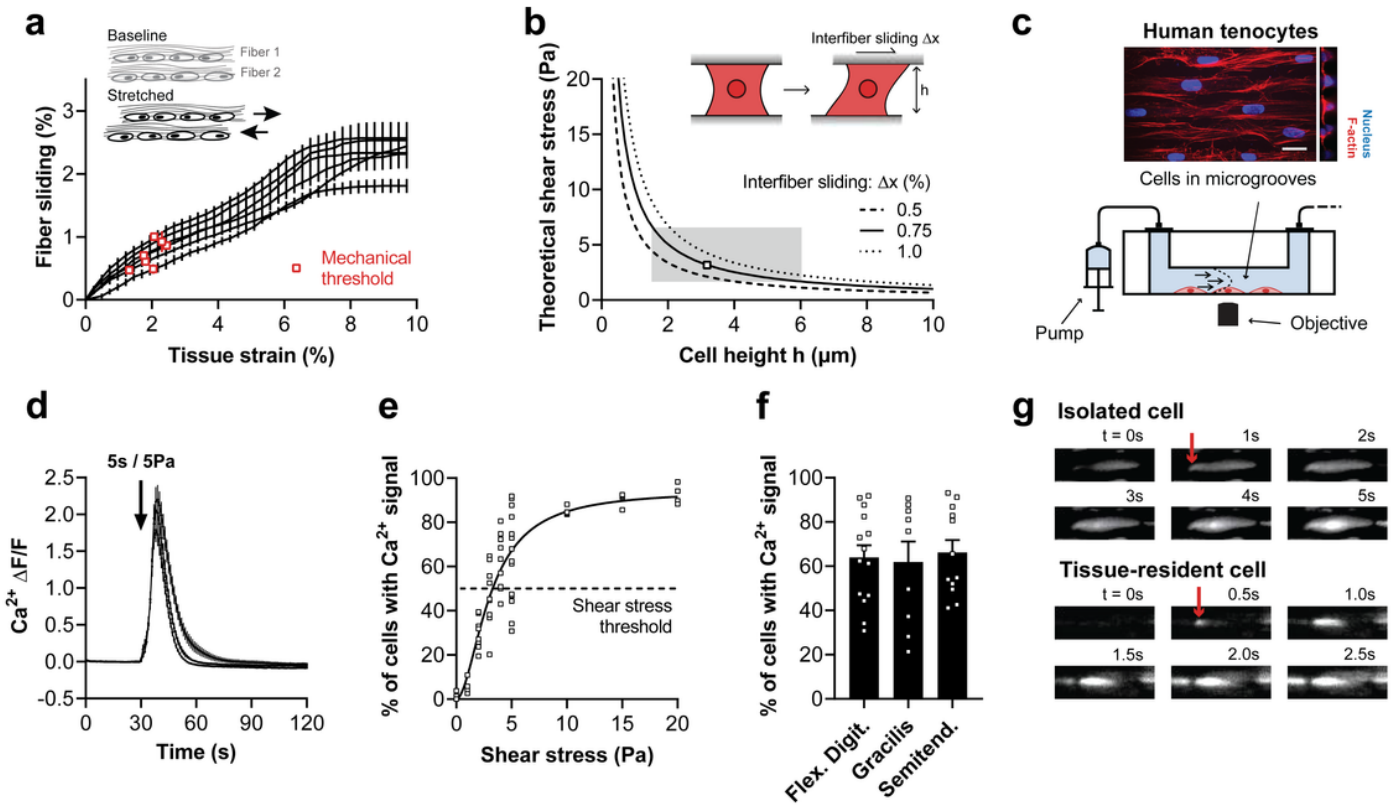

Figure 2

Shear stress as a key stimulus driving Ca2+ signals in isolated tenocytes. (a) Fiber sliding quantified from cell displacements occurring in fascicles stretched at low strain rate (n=7 fascicles). (b) Theoretical shear stresses acting on tenocytes due to inter-fiber sliding and the predicted mechanosensitive zone of tenocytes (gray box). (c) Schematic of flow chamber with aligned micro-channels to promote a native cell morphology used for Ca2+ imaging of isolated tenocytes during shear stress stimulations (scale bar, 20 μm). (d) Shear stress (5 Pa for 5 s, onset indicated by arrow) induces Ca2+ signals in human tenocytes (n=12 chambers, cells from 3 human donors). (e) Tenocytes display increased response rate with increasing shear stress (for each condition n≥4 chambers, cells from 2 human donors), nonlinear fit with Hill slope, y=(94.42 * x^h)/(〖3.08〗^h + x^h) ; h = 1.854 ; R2 = 0.862. (f) No difference in shear stress (5 Pa for 5 s) response in tenocytes from different anatomical locations (for each condition n≥9 chambers, cells from 2-3 human donors), one-way ANOVA with multiple comparisons (Tukey's test). (g) Representative Ca2+ signals originating at cell periphery (indicated by arrow) both in vitro (shear stress) and in situ (tissue stretch). Data are means±s.e.m., **p<0.01, ***p<0.001.

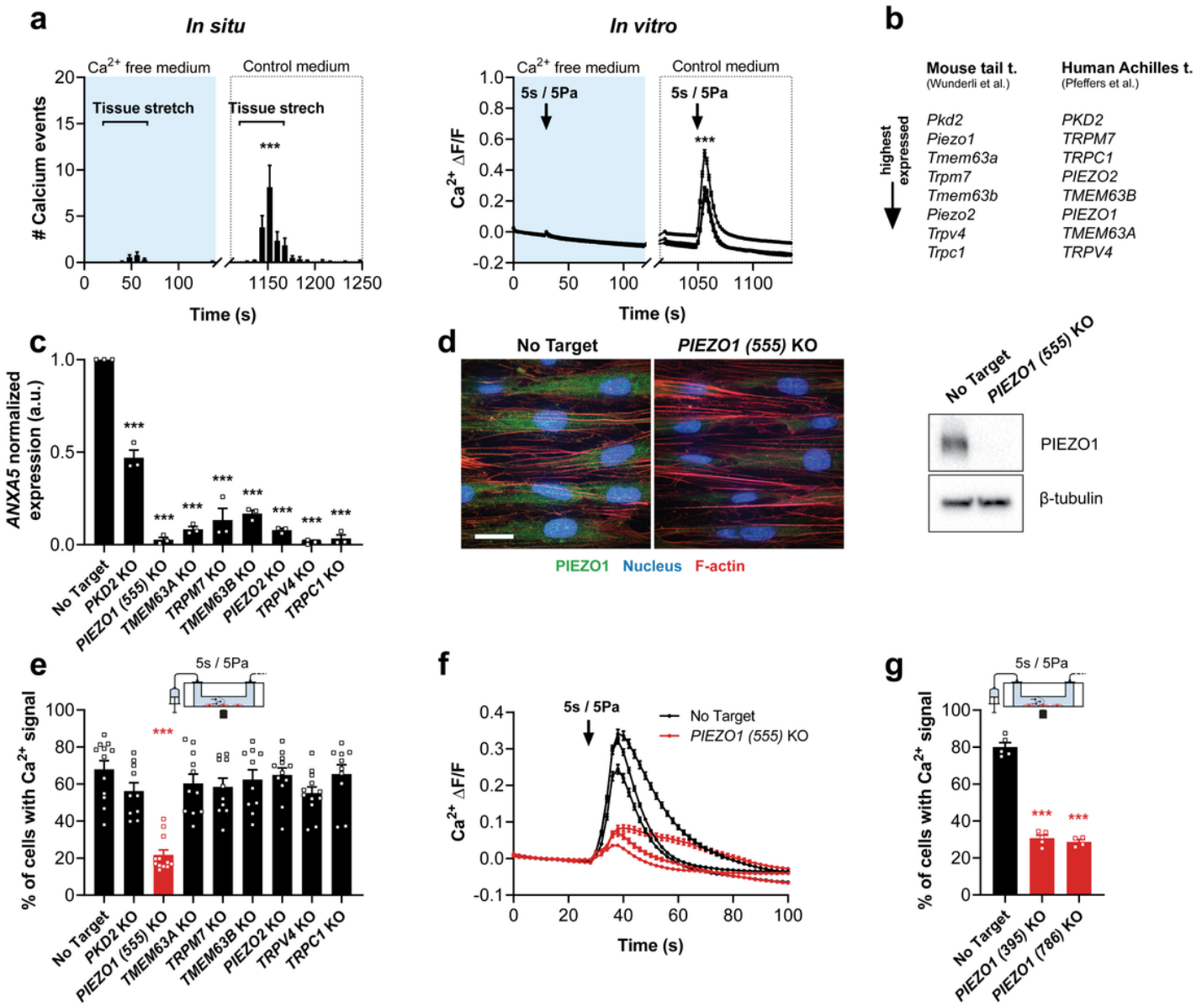

Figure 3

PIEZO1-mediated shear stress response in human tenocytes. (a) Mechanically-induced Ca2+ signals are nearly absent in Ca2+-free medium (containing 2 mM EGTA and 2 mM MgCl2 instead of CaCl2) but are restored in control medium, both in situ (one cycle stretch to 2.7% strain at 0.1% strain/s, n=7 fascicles from rat tails) and in vitro (shear stress stimulation, n=12 chambers, cells from 3 human donors), paired Student's t-test. (b) Highest expressed candidate genes associated with mechanosensitive ion channel characteristics selected from RNA sequencing experiments with tendons. (c) CRISPR/Cas9-mediated knockout efficiency of candidate genes, normalization to gene expression in no target cells using 2−ddCT method (cells from n=3 human donors), one-way ANOVA with multiple comparisons (Dunnett's test). (d) Immunofluorescence images and Western blot analysis showing efficient PIEZO1 knockout in human tenocytes (scale bar, 20 µm). (e) PIEZO1 depleted cells show reduced % of cells responding to 5 Pa shear

stress for 5 s (for each condition n≥10 chambers, cells from 3 human donors, one-way ANOVA with multiple comparisons, Dunnett's test) and (f) diminished intracellular Ca2+ response (averaged over all single segmented cells). (g) Two additional PIEZO1 knockouts generated with different CRISPR-guide-RNAs confirm the reduced shear stress response, one-way ANOVA with multiple comparisons (Dunnett's test). Data are means±s.e.m., ***p<0.001.

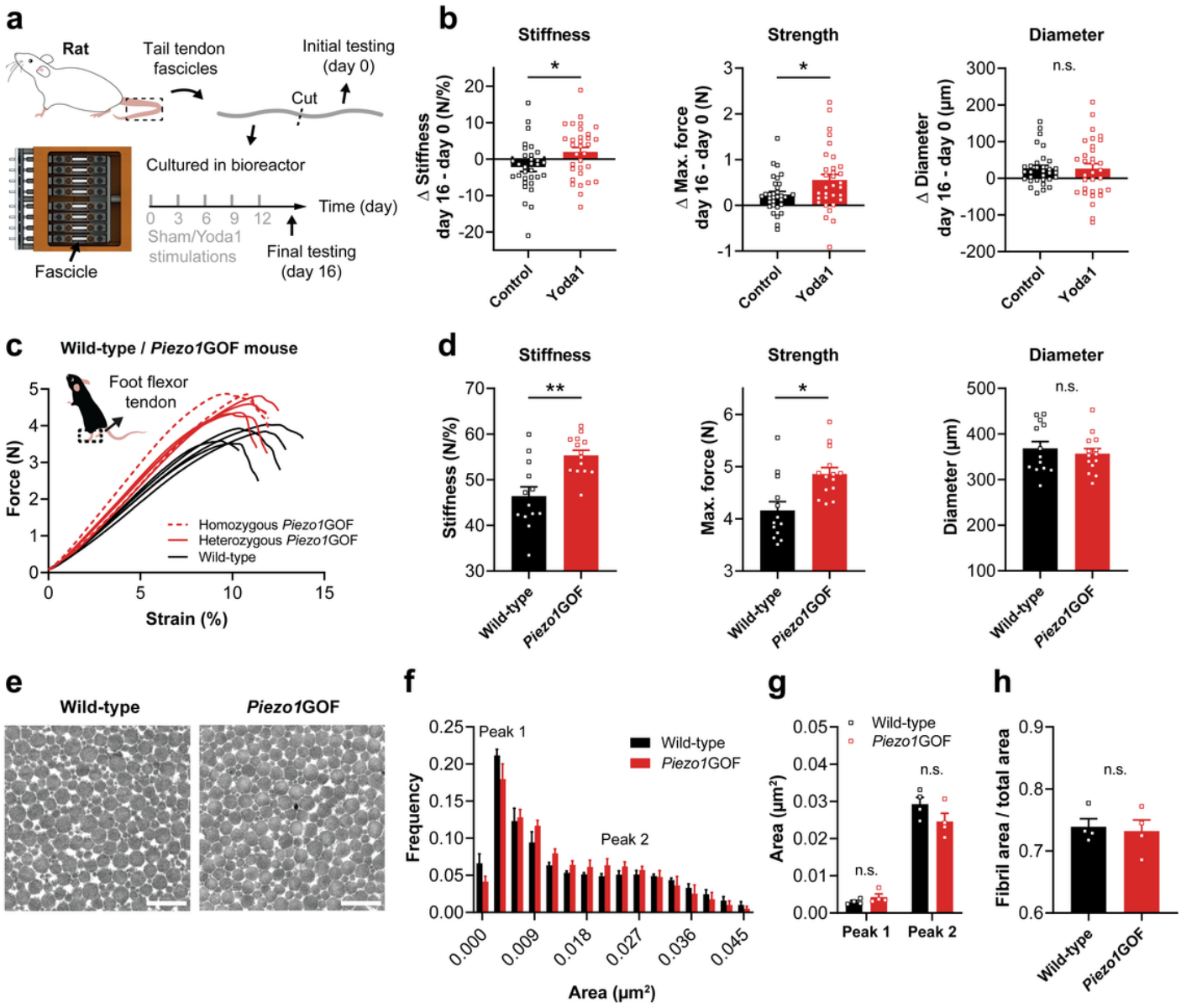

Figure 4

Stiffness and strength regulation of murine tendons by PIEZO1. (a) Schematic of in vitro experiment with tendon explants subjected to sham or 5 µM Yoda1 stimulation. (b) Biomechanical characterization of tendon explants (ramp-to-failure tests) shows higher stiffness and strength after Yoda1-treatment, with no difference in diameter (n=32 fascicles, 4 rats), Mann-Whitney test. (c) Ramp-to-failure curves of plantaris tendons from littermates demonstrate a tendon phenotype in constitutive Piezo1GOF mice (GOF

mutation in all tissues) with (d) increased stiffness and strength but unaffected diameter, n=8 Piezo1GOF mice (6 heterozygous and 2 homozygous Piezo1GOF) and n=7 wild-type littermate controls were analyzed from 3 litters in total, differences were examined using linear mixed effects models. (e) TEM images of plantaris tendon collagen fibrils (scale bar, 500 nm). (f) Frequency distribution of collagen fibril area obtained from TEM images of plantaris tendons is similar between groups, an average of around 23’600 collagen fibrils were analyzed per tendon (one tendon per mouse, n=4 mice per genotype). (g) No differences were observed in the two local peaks determined with a fit of the frequency distribution (n=4 mice per genotype, multiple t-tests) and (h) in tissue compactness (n=4 mice per genotype, unpaired Student’s t-test). Data are means±s.e.m., n.s. not significant, * p<0.05, **p<0.01.

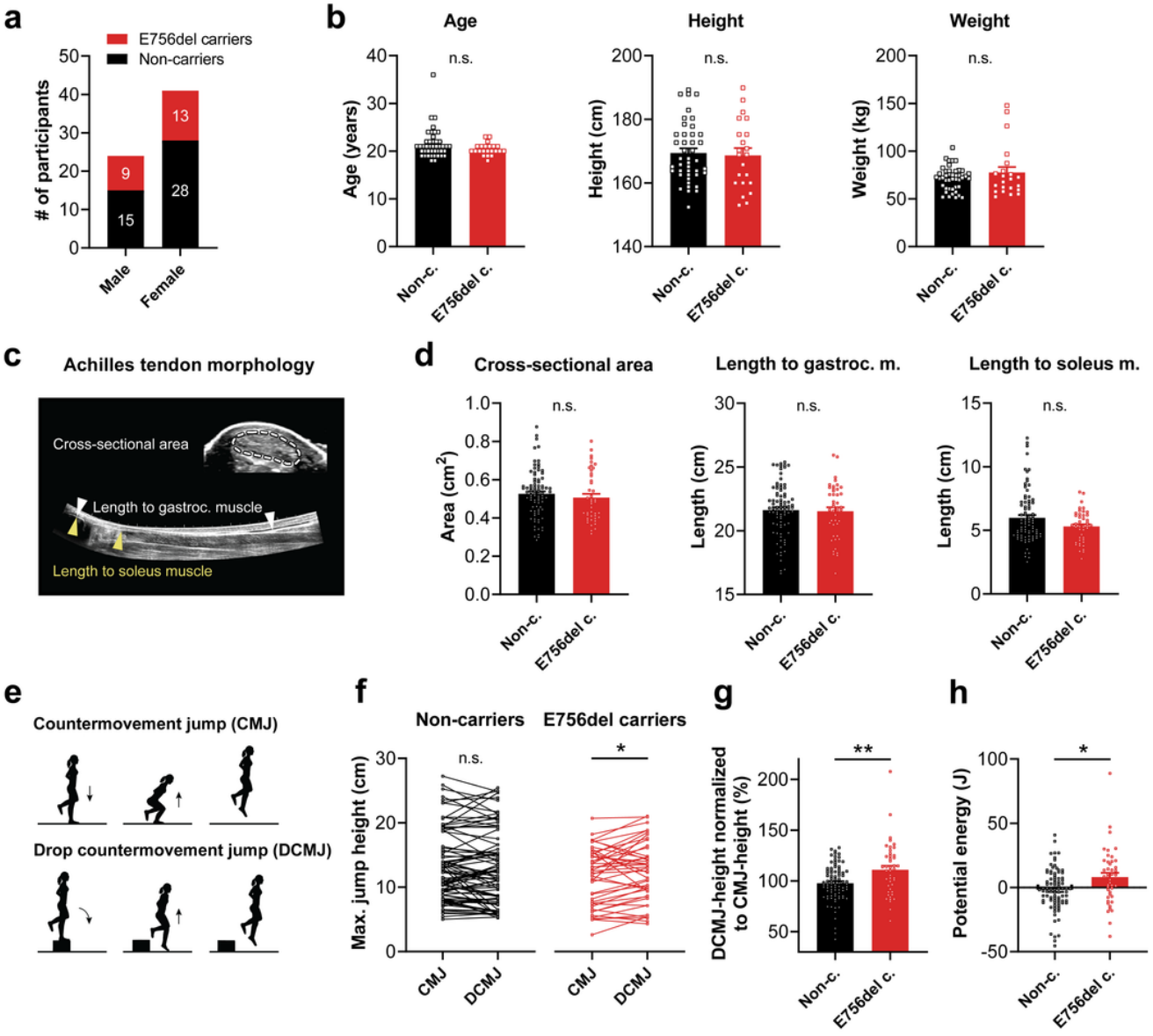

Figure 5

Human jumping performance influenced by PIEZO1GOF E756 mutation with no effect on Achilles tendon morphology. (a) n=22 E756del carriers and n=43 non-carriers identified in 65 African American participants with (b) no differences in age, height and weight between the two groups, Mann-Whitney test. (c) Ultrasound-based morphological assessment of the Achilles tendon. (d) Unaffected Achilles tendon cross-sectional area, length to gastrocnemius muscle and to soleus muscle by E756del mutation. (e) Schematic of single leg countermovement jump (CMJ), and single leg drop countermovement jump (DCMJ) used to assess jumping performance; CMJ and DCMJ differ by initial drop in DCMJ, which leads to greater Achilles tendon loading; for each leg and jump the average of 3 trials was used for analysis. (f) Non-carrier controls show no difference in maximal jumping height between CMJ and DCMJ, in contrast E756del carries perform significantly better in DCMJ compared to CMJ. (g) Normalization of DCMJ- to CMJ-height, to isolate the effect of greater tendon loading, shows significant increase in normalized jumping height in E756del carriers compared to non-carriers. (h) Conversion of jump height difference (between DCMJ and CMJ) into potential energy demonstrates that E756del carriers more effectively transformed drop energy into jump height. Statistics performed with linear mixed effects models unless indicated otherwise, both legs of n=22 E756del carriers and n=43 non-carriers were analyzed. Data are means±s.e.m., n.s. not significant, * $p<0.05$, ** $p<0.01$.

Supplementary Files

This is a list of supplementary files associated with this preprint. Click to download.

- TableS1.xlsx
- TableS2.xlsx
- MovieS1aBaseline.mov
- MovieS1bStretched.mov
- MovieS2aFLIMBaseline.avi
- MovieS2bFLIMPoststretch.avi
- MovieS3ShearstressResponseinIsolatedCells.mov
- MovieS4Yoda1stimulation.mov
- FigureS1.png
- FigureS2.png
- FigureS3.png
- FigureS4.png
- FigureS5.png